Dynamic Capabilities of Multi-MHz Inductive Power Transfer Systems Demonstrated With Batteryless Drones

Juan M. Arteaga, Samer Aldhaher, George Kkelis, Christopher Kwan, David C. Yates, *Member, IEEE*, and Paul D. Mitcheson, *Senior Member, IEEE*

***Abstract*—This paper presents the design of a multi-MHz inductive power transfer (IPT) system showcasing lightweight and energy-efficient solutions for non-radiative wireless power transfer. A proof of concept is developed by powering a drone without a battery that can hover freely in proximity to an IPT transmitter. The most challenging aspect, addressed here for the first time, is the complete system-level design to efficiently provide uninterrupted power flow while allowing for variable power demand and highly variable coupling factor. The proposed solution includes the design of lightweight air-core coils that can achieve sufficient coupling without degrading the aerodynamics of the drone, and the design of newly developed resonant power converters at both ends of the system. At the transmitting-end, a load-independent Class EF inverter, which can drive a transmitting-coil with constant current amplitude and achieves zero-voltage switching for the entire range of operation, was developed; and at the receiving-end, a hybrid Class E rectifier, which allows tuning for large changes in coupling and power demand, was used. For the demo, the range of motion of the drone was limited by a 7.5 cm nylon string tether, connected between the center of the transmitting-coil and the bottom of the drone. The design of the IPT system, including all the power conversion stages and the IPT link, is explained in detail. The results on performance and specific practical considerations required for the physical implementation are provided. An average end-to-end efficiency of 60% was achieved for a coupling range of 23%–5.8%. Relevant simulations concerning human exposure to electromagnetic fields are also included to assure that the demo is safe, according to the relevant guidelines. This paper is accompanied by a video featuring the proposed IPT system**

Manuscript received June 15, 2018; revised August 9, 2018; accepted September 13, 2018. Date of publication September 19, 2018; date of current version April 20, 2019. This work was supported in part by the Department of Electrical and Electronic Engineering, Imperial College London, in part by the PINN Programme, Ministry of Science and ICT of Costa Rica MICITT, in part by the University of Costa Rica, in part by the U.K. Government, and in part by the EPSRC Converter Architectures under Grant EP/R004137/1. Recommended for publication by Associate Editor A. Khaligh. *(Corresponding author: Juan M. Arteaga.)*

J. M. Arteaga, S. Aldhaher, C. Kwan, D. C. Yates, and P. D. Mitcheson are with the Department of Electrical and Electronic Engineering, Imperial College London, London SW7 2AZ, U.K. (e-mail: j.arteaga-saenz15@imperial.ac.uk; s.aldhaher@imperial.ac.uk; christopher.kwan09@imperial.ac.uk; david.yates@imperial.ac.uk; paul.mitcheson@imperial.ac.uk).

G. Kkelis is with TMD Technologies Ltd., Hayes UB3 1DQ, U.K. (e-mail: gmkkelis@gmail.com).

This paper has supplementary downloadable material available at http://ieeexplore.ieee.org, provided by the authors.

Color versions of one or more of the figures in this paper are available online at http://ieeexplore.ieee.org.

Digital Object Identifier 10.1109/TPEL.2018.2871188

***Index Terms*—Inductive power transmission, unmanned aerial vehicles, wireless power transmission.**

I. Introduction

THE possibility of wirelessly powering electric unmanned aerial vehicles (UAVs) was first demonstrated in [1]. The means by which power was transferred to the UAV, hovering 15 m above the ground, was a 2.45-GHz microwave beam generated by a 5-kW magnetron, from which the UAV was able to pick up a maximum of 270 W. Encouraged by this impressive precedent from 1969, we developed a wireless power transfer system to wirelessly power a UAV, using not a microwave beam but inductive coupling, a non-radiative wireless power transfer solution that has been widely proposed to wirelessly charge electric vehicles [2]–[4]. Our demo uses a smaller UAV than the one in [1], and the wireless gap is shorter. However, inductive power transfer (IPT) allows for efficiencies higher than 90% to be achieved [5], [6] and could, therefore, become a normal solution to charge such vehicles.

IPT can be performed efficiently at low coupling if the Q-factor of the coils is high. In [7], this capability was showcased: A light bulb was powered wirelessly using self-resonant coils, where the separation between the source and the load was reported to be of four-coil diameters. Various techniques to optimize the link were, then, formulated in [8], and by implementing this theory at multi-MHz frequencies, significant improvements in end-to-end efficiencies have been achieved. For example, in [9], a dc–ac efficiency of 77% was reported at 6 MHz and 3.5% coupling, and most recently, in our previous work [10], we achieved 88% dc–dc efficiency at 6.78 MHz and 10.5% coupling. The introduction of wide bandgap devices has also pushed the capabilities and end-to-end efficiencies of these systems forward. For example, in [11], a 13.56-MHz coil driver with a 1.3-kW power capability was developed using a gallium nitride (GaN) transistor as the switching device.

One of the biggest challenges addressed in [1], which has also been identified in more recent wireless power transfer (WPT) systems proposed to wirelessly charge UAVs [12], is dealing with wireless power transfer and variable position. Solutions for variable coupling have been proposed for dynamic electric vehicle (EV) charging IPT systems that operate at kilohertz frequencies: Power throughput control is implemented either at the

transmitting-end by regulating the transmitting-coil current [13], at the receiving-end by changing the load impedance [14], or as a combination of the two [15]. Interestingly, systems with power throughput control only at the receiving-end do not require a communication link between both ends of the system since they can operate at constant amplitude current in the transmitting coil.

Increasing the frequency of operation to the megahertz range and, therefore, relying on resonant power converter topologies at one or both ends of the system limits the capabilities for power throughput control directly on the power converters, since variables such as the duty cycle, frequency, and, sometimes, the load resistance not only determine the power throughput but also the soft switching [16]. Hence, when employing resonant converters, power throughput control is often performed by additional power conversion stages, either at the transmitting-end before the inverter or at the receiving-end after the rectifier. Solutions for variable coupling using multi-MHz resonant power converters can be found in [10] and [17].

The improvements in power capability, end-to-end efficiency, and tolerance to variable coupling have significantly increased the viability of implementing multi-MHz IPT systems for wireless charging in a variety of applications, an example of which is the wireless charging for UAVs. Considering the vast range of applications for UAVs [18], we developed a demo that is capable of wirelessly powering a drone without a battery, while it hovers close to a charging pad to showcase features that are beneficial, and in some cases necessary, to wirelessly power or charge dynamic loads, such as a hovering UAV.

This paper is organized as follows. Section II gives a system overview and Section III gives an overview of the IPT theory, highlighting the theoretical possibilities and limitations of this technology when considering spatial freedom. The requirements for the design of the coils are, then, determined in Section IV, considering the physical constraints and the range of motion of the system. Section V examines electromagnetic exposure guidelines to humans by performing simulations in order to verify the safety aspect of the demo and, if necessary, to restrain the current levels in the coils. The design of the inverter, a load-independent Class EF, is then proposed in Section VI to cope with the highly varying coupling of this application. Then, the design of a hybrid Class E rectifier that can cope with the variable loading conditions is presented in Section VII. Section VIII revises the dynamics and comments on the performance of the system. Section IX reviews additional prototypes created and comments on the possible future applications of this technology. Section X concludes this paper.

Some aspects of the design of this system have been published in our earlier work. A first prototype, which operates in a narrow range in coupling, was presented in [19], and the probability distribution of the IPT environment was presented in [20]. Additionally, an alternative design of the rectifier, mentioned in Section IX, using a synchronous Class E rectifier, was presented in [21] and [22].

II. System Overview

The UAV model implemented is a Hubsan H107L X4 quadcopter. This commercially available drone comes with a lithium polymer battery that outputs a voltage of 3.7–4.2 V, depending on the state of charge. At full throttle, the motors of the drone draw approximately 13 W from the source. We replaced the battery with an IPT receiver, enabling the drone to operate without an energy storage system in proximity to the IPT transmitter; this was done to demonstrate the capabilities of the technology in handling a variable load with a variable position. Fig. 1 shows a photograph of the demo, including the Hubsan H107L X4 quadcopter, with an on-board IPT receiver instead of a battery.

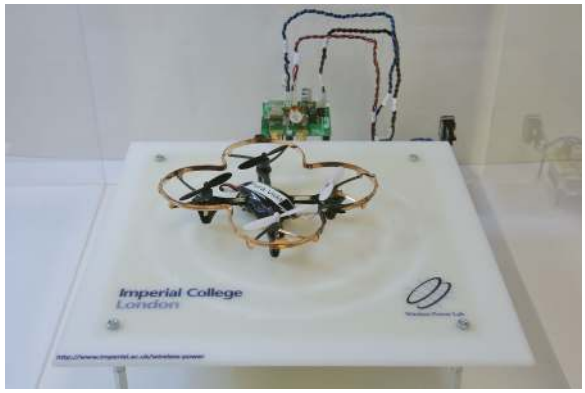

Fig. 1. Photograph of the wirelessly powered drone.

The selected frequency of operation was 13.56 MHz because the design of the coils (size, shape, and weight), especially the one on the drone, is very restrictive. The option of including magnetically permeable materials was dismissed since these would add weight and, most likely, interfere with the air-flow of the propellers. Also, a planar coil with multiple turns would produce similar disadvantages at the receiver side. The benefit of operating at 13.56 MHz is that a single-turn air-core coil of roughly 10 cm diameter produces a sufficiently large reactance to load the transmitting-end, and therefore supply the power demand of the drone at minimum coupling, which for this experiment was 5.8%.

The wireless power transfer design presented in this paper was built to highlight the possibilities of motion and good efficiency of multi-MHz IPT systems, while also demonstrating its feasibility to be showcased outside the laboratory. The demo has been shown at the Applied Power Electronics Conference 2017, the Centre for Power Electronics UK Annual Conference 2017, the PCIM Europe 2017, and the Wireless Power Week 2018. The design, implementation, and analysis of the demo are introduced here.

III. IPT for Systems With Variable Coupling Factor

A two-coil IPT system can be represented with the block diagram shown in Fig. 2 and the circuit diagrams shown in Fig. 3. Fig. 2 depicts the conversion from a dc voltage at the input V_{dc} to a high-frequency current i_{p} in the transmitting-coil, which produces an electromotive force $\mathcal{E}_{\mathrm{s}}$ at the receiving-coil; this voltage is, then, rectified V_{o} and, finally, regulated by a dc–dc converter $V_{\mathrm{o_{reg}}}$. Fig. 3 shows the equivalent circuits used to represent an IPT link, where the IPT coils' inductances are represented by L_{p} and L_{s}, and their equivalent series resistances

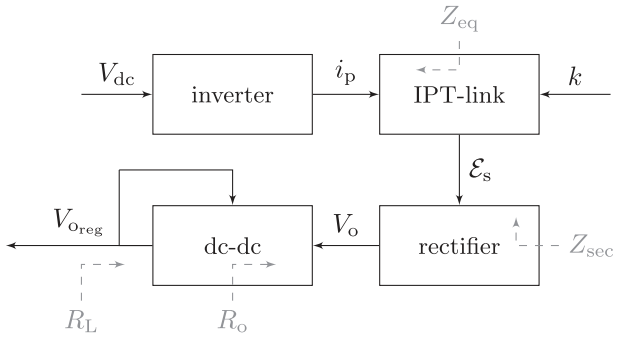

Fig. 2. Power flow diagram of an IPT system with variable coupling.

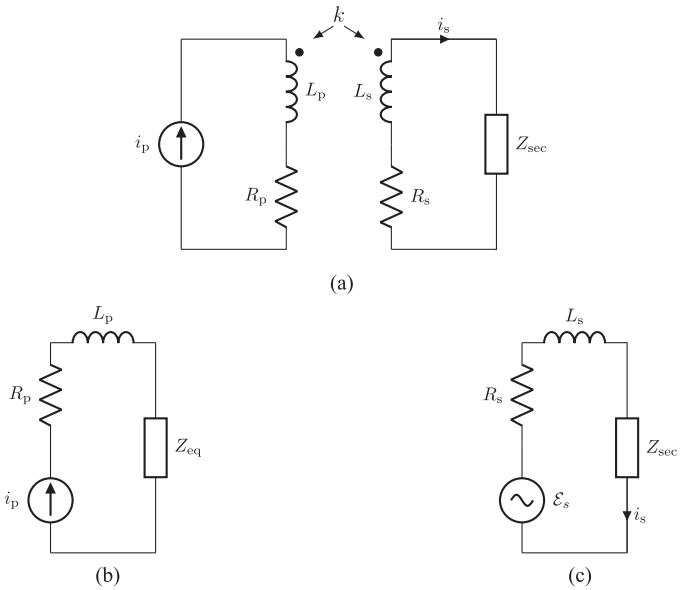

Fig. 3. Equivalent circuits of an IPT system. (a) IPT system. (b) Transmitting-end. (c) Receiving-end.

by $R_{\rm p}$ and $R_{\rm s}$, respectively. The rectifier's input impedance is $Z_{\rm sec}$, as shown in Fig. 3, and $Z_{\rm eq}$ is the reflected impedance on the transmit side.

The IPT-link block shown in Fig. 2 represents the exchange of power between the transmitting and receiving coils ($L_{\rm p}$ and $L_{\rm s}$ shown in Fig. 3), where the coupling factor k, a function of the mutual inductance $M_{\rm ps}$, defined by

$$k = \frac{M_{\rm ps}}{\sqrt{L_{\rm p} L_{\rm s}}} \tag{1}$$

depends on the relative position of the coils [23]. k is defined as an input to the system to investigate the effects produced by changes in the relative position of the coils over time.

The other input to the IPT-link block is $i_{\rm p}$, which is the amplitude of the alternating current fed to the transmitting-coil by the inverter. Here, we consider the frequency of the output current of the inverter $f_{\rm i_p}$ as a constant, typically 6.78 or 13.56 MHz, which are the first two industrial, scientific and medical (ISM) bands and at which the majority of multi-MHz IPT systems operate.

The induced electromotive force in the receiving coil $\mathcal{E}_{\rm s}$ is defined as the output of the IPT-link block and the input of the rectifier. Here, we consider $L_{\rm s}$ as a constant and the external capacitance, usually implemented to resonate the receiving coil, as part of the rectifier. $\mathcal{E}_{\rm s}$ can be calculated [1] as follows:

$$\boldsymbol{\mathcal{E}_{\rm s}} = \boldsymbol{j} 2\pi f_{\rm i_p} k \sqrt{L_{\rm p} L_{\rm s}} \boldsymbol{i_{\rm p}}. \tag{2}$$

On the primary side, the influence of the receiving-end is represented by a reflected impedance $\boldsymbol{Z_{\rm eq}}$, which can be formulated as a function of the input impedance of the rectifier $\boldsymbol{Z_{\rm sec}}$ shown in Fig. 3. Considering $\boldsymbol{Z_{\rm sec}} = R_{\rm sec} + \boldsymbol{j} X_{\rm sec}$ and $\boldsymbol{Z_{\rm eq}} = R_{\rm eq} + \boldsymbol{j} X_{\rm eq}$, we obtain

$$R_{\rm eq} = \frac{4\pi^2 f_{\rm i_p}^2 k^2 L_{\rm p} L_{\rm s} \left(R_{\rm s} + R_{\rm sec}\right)}{\left(R_{\rm s} + R_{\rm sec}\right)^2 + \left(2\pi f_{\rm i_p} L_{\rm s} + X_{\rm sec}\right)^2} \tag{3}$$

$$X_{\rm eq} = -\frac{4\pi^2 f_{\rm i_p}^2 k^2 L_{\rm p} L_{\rm s} \left(2\pi f_{\rm i_p} L_{\rm s} + X_{\rm sec}\right)}{\left(R_{\rm s} + R_{\rm sec}\right)^2 + \left(2\pi f_{\rm i_p} L_{\rm s} + X_{\rm sec}\right)^2}. \tag{4}$$

This formulation allows the circuits at both ends of the system to be designed separately, while accounting for changes in k.

A. *Effects of Variable Coupling on Output Power*

The effects of variations in power demand and coupling can be described at the transmitting-end using the equivalent circuit models shown in Fig. 3. The power dissipated in the reflected resistance $R_{\rm eq}$ represents the power dissipated in the load $P_{\rm o}$, which varies in accordance with the power demand, and the losses in all power conversion stages at the receiving-end. Thus, we have

$$\frac{P_{\rm o}}{\eta_{\rm r}} = \frac{i_{\rm p}^2 R_{\rm eq}(k, \boldsymbol{Z_{\rm sec}})}{2} \tag{5}$$

where $\eta_{\rm r}$ is the efficiency of the receiving-end, which accounts for the losses in the receiving coil, the rectifier, and the dc–dc converter.

The output power of an IPT system with a given set of coils and a fixed frequency of operation changes in accordance with (3) and (5) with the following variables: k, $i_{\rm p}$, $R_{\rm sec}$, and $X_{\rm sec}$. The value of k is bounded ($k_{\rm min}$ and $k_{\rm max}$) in accordance with the range of motion of the system, and the other three variables can potentially be utilized to regulate power as the position of the coils change.

Controlling power throughput at the transmit side by varying $i_{\rm p}$ is possible with a wireless communication link between the transmitter and receiver. This, however, adds complexity to the system and its dynamics. Such a system would require an additional power conversion block at the input of the inverter, or the implementation of an inverting topology where the output current depends on a variable other than the input voltage. Varying $\boldsymbol{Z_{\rm sec}}$ ($R_{\rm sec}$ and $X_{\rm sec}$ shown in Fig. 3) is the other alternative to control power throughput, with the benefit of having a single control stage close to the load at the receiving-end and not requiring feedback between the receiving-end and the transmitting-end. Its main limitation, however, is that a system that changes the input impedance of the rectifier to control

[1] Complex phasor quantities are marked as bold.

power throughput cannot be optimized for maximum link efficiency over the entire range of k and $P_{\rm o}$; first, this is because if $X_{\rm sec}$ is not equal to $-2\pi f_{\rm i_p} L_{\rm s}$, the power factor at $\mathcal{E}_{\rm s}$ is different than one, i.e., the same amount of power could be delivered to the load with a lower current in the receiving coil and, therefore, lower losses in $R_{\rm s}$. Second, if $R_{\rm sec}$ is not equal to the optimal load, which is the value of $R_{\rm sec}$ that achieves the minimum losses in $R_{\rm p}$ and $R_{\rm s}$ in proportion to $P_{\rm o}$ [8], then one of the coils will have a higher than optimal circulating current, resulting in higher losses in the IPT-link.

B. Integration of a DC–DC Converter for Power Throughput Control

To vary $\boldsymbol{Z_{\rm sec}}$, a pulsewidth modulation based dc–dc converter is integrated as the last power conversion stage at the receiving end, as can be seen in the diagram shown in Fig. 2, to regulate the output voltage with duty cycle $\delta_{\rm dc-dc}$. As a consequence, the dc–dc converter's input resistance $R_{\rm o}$ changes with its input voltage (or the rectifier's output voltage $V_{\rm o}$) and its load resistance ($R_{\rm L}$) as follows:

$$R_{\rm o} = \eta_{\rm dc-dc} \left(\frac{V_{\rm o}}{V_{\rm o_{reg}}(\delta_{\rm dc-dc})} \right)^2 R_{\rm L} \tag{6}$$

where $\eta_{\rm dc-dc}$ is the efficiency of the dc–dc converter and $V_{\rm o_{reg}}$ is the regulated output voltage.

This raises challenges for the rectifier design because it must operate at highly variable input voltages (2) and at variable load resistances (6). In addition, the range of $V_{\rm o}$ has to be limited not only by the ratings of the components of the rectifier but also by the range of input voltages supported by the dc–dc converter.

C. Electric Dynamics of the System

The dynamics can be analyzed at both ends of the system separately when the inverter is load-independent [21], given that this feature decouples the design of both ends of the system. However, at the transmit side, $R_{\rm eq}$ and $X_{\rm eq}$ can reach values beyond the range of steady-state operation as the system enters a transient, which may temporarily overload the inverter and produce unwanted changes in the behavior of $i_{\rm p}$ or, in some cases, surpass the ratings of the devices in the inverter. Since there is no feedback-loop required at the transmit side to regulate power throughput, the dynamics of the transmitting-end have to be considered solely for the design of the input filter and the maximum ratings of the devices for step changes in k and $R_{\rm L}$.

At the receiving-end, the response of $V_{\rm o}$ has to be considered as a consequence of a step change in $i_{\rm p}$, k (or $\mathcal{E}_{\rm s}$ representing both), and $R_{\rm L}$. The behavior of the dc–dc converter and the design of the filters determine whether the system remains stable over the entire operating range of k and $R_{\rm L}$.

IV. Design of the IPT-Link

The receiving coil in this application is one of the most restrictive elements in the design. It should be very lightweight and the electric and magnetic conductors that comprise the coil should not interfere with the aerodynamics of the drone.

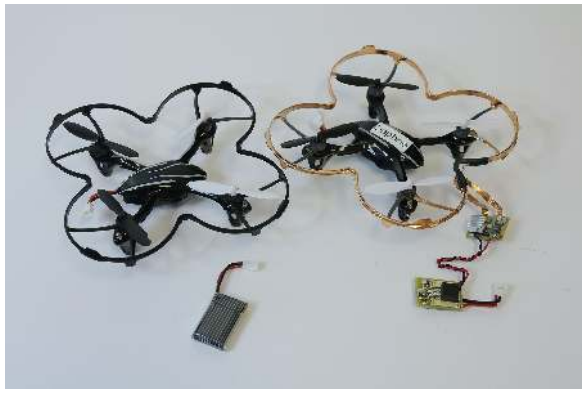

Fig. 4. Photograph of the off-the-shelf drone with its battery (left) next to the modified drone with a plated copper coil, the rectifier board, and the dc–dc converter (right).

The size and shape of the coils also determine the coupling distribution in space, confining a range of motion for a given range of k. The design of the transmit coil is less restrictive since the weight and aerodynamics are not as crucial as in the receiver coil. Nonetheless, a system in which the transmitting-end is mounted on a drone is discussed in Section IX.

A. Design of the IPT Coils

The receiving air-core coil was fabricated by copper-plating a plastic structure with the shape of the propeller guard of the drone, as shown in Figs. 4 and 5. This minimizes the effect of the coil on the aerodynamics of the drone and, at the same time, achieves high coupling ($k > 5\%$) over a broad range of distance and misalignment due to the large loop area of the coil.

It was verified in previous experiments on the unmodified drone that the presence of the magnetic field generated by the proposed IPT transmitter had no effect on the flying controls and also did not produce heating anywhere in the drone.

The transmitting-coil consists of a two-turn circular printed circuit board coil with an external diameter of 20 cm and no magnetically permeable materials. The shape of this coil, previously characterized in [24], can be seen in Fig. 5. Both coils were simulated using Computer Simulation Technology (CST) and measured with a Keysight E4990A impedance analyzer. It should be noted, however, that the equivalent-series-resistance (ESR) of high-Q coils is very difficult to measure accurately [25], and therefore, the values from simulations are preferred over measurements for the design of the inverter and the rectifier. The specifications of the coils are presented in Table I, and the coils diagrams are shown in Fig. 5.

B. Range of Motion and Variable Coupling

The range of motion of the system was limited by anchoring the drone to the center of the charging pad with a nylon string tether. The maximum coupling $k_{\rm max}$ takes place when the drone sits on top of the transmitting coil with the coils perfectly aligned, and the minimum coupling $k_{\rm min}$ when the drone hovers far from the transmitter at maximum separation. Coupling depends on the length of the tether r, as shown in Fig. 6, and the angle θ, which determines the misalignment.

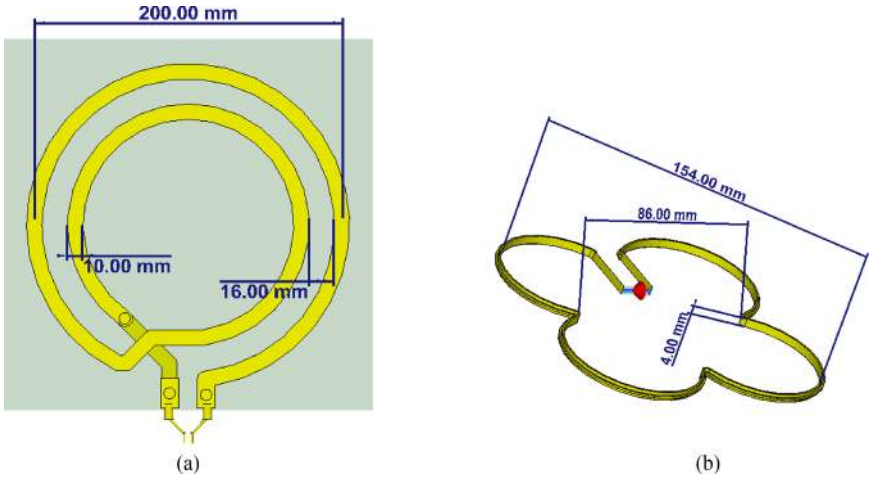

Fig. 5. Coils diagrams. (a) Transmitting coil. (b) Receiving coil.

TABLE I
SPECIFICATIONS OF THE COILS AT 13.56 MHz

	Transmitting coil	Receiving coil
Shape	Circular planar	Drone's propeller guard
External Diameter [cm]	20	9-16
Number of turns	2	1
Measured inductance [nH]	1181.0	379.9
Simulated inductance [nH]	1155.7	392.0
Measured resistance [mΩ]	202.7	103.9
Simulated resistance [mΩ]	191.2	89.0
Measured unloaded Q	496	312
Simulated unloaded Q	515	375

The maximum simulated coupling was 23.7%; however, the maximum measured coupling did not exceed 20% at any point throughout the range of motion. The length of the tether was set at 7.5 cm in order to have a minimum coupling higher than 5%. The minimum coupling was simulated and measured at 5.8% when $r = 7.5$ cm and $\theta = 0°$. The distribution of k in space is shown as a color map in Fig. 7, obtained from simulations using CST.

If no external control over the flight operation of the drone is performed, then its position in time is unpredictable and cannot be described analytically. This is the case for the demo that was built. It is operated at maximum throttle with no external control over its direction, which tends to vary unpredictably. The drone's position can, however, be analyzed as a stochastic variable and characterized using statistical data. The position of the drone was monitored and presented as a probability distribution of k over time in [20]. Fig. 8 shows the distribution of k as a histogram with equal size bins of 0.5% coupling, when the drone is at maximum throttle and has no external flight control.

Characterizing motion as a probability distribution is useful because it allows optimizing for the link and the circuits at both ends of the system for maximum overall energy efficiency, as proposed in [10].

V. SYSTEM DESIGN IN ACCORDANCE WITH ELECTROMAGNETIC EXPOSURE GUIDELINES

The design of an IPT system that operates in proximity to human beings has to be done in accordance with the guidelines on human exposure to electromagnetic fields. In IPT, since a high-frequency magnetic field is the means by which power is transferred, the potential adverse health effects that could arise mainly from interactions between the human tissue and magnetic field have to be analyzed.

The International Commission on Non-Ionizing Radiation Protection has published a widely accepted set of guidelines to minimize the risk of human exposure to electromagnetic fields [26], [27]. For frequencies higher than 100 kHz, which is the range relevant to this paper, the exposure limits are specified in [26]. At frequencies higher than 10 MHz, only thermal effects are considered to be of risk, and therefore, the only restrictions are based on the specific absorption rate (SAR). Table II presents the SAR limits specified in [26], which also coincide with the regulations in the IEEE C39.1-2005 standard [28] at frequencies higher than 100 kHz.

Despite both [26] and [28] giving different incident reference field levels that assure compliance with the SAR limits specified in Table II for the worst case scenario, they are more appropriate when designing an IPT application to evaluate exposure limits using SAR simulations [29], [30]. We performed SAR simulations using three-dimensional electromagnetic simulation software at the critical points of operation in terms of exposure of the wirelessly powered drone demo, which is designed to be enclosed in a cubic Perspex box 40 cm wide. The simulation results at the two most critical points are shown in Fig. 9, considering i_{p} equal to 5.5 A, which is the worst case among the viable solutions to power the drone efficiently.

The simulations show that the highest localized SAR value from simulation is 0.00199047 W/kg, which is more than a

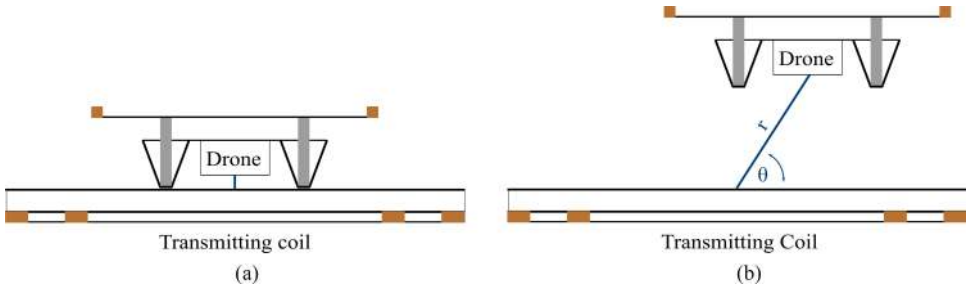

Fig. 6. Cross section of the IPT-link describing the range of motion of the system. (a) Maximum coupling. (b) Low coupling.

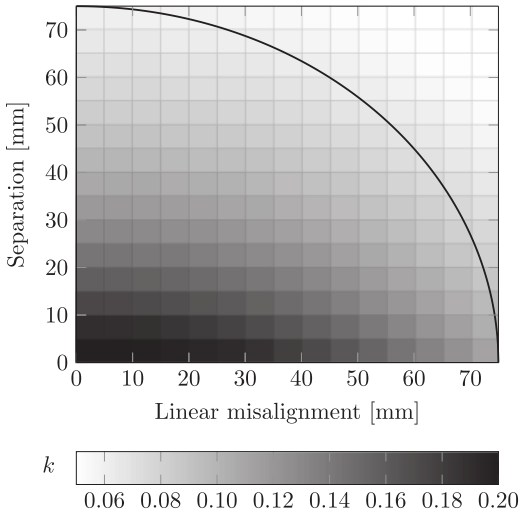

Fig. 7. Distribution of k throughout the range of motion, limited by a 7.5 cm string tether.

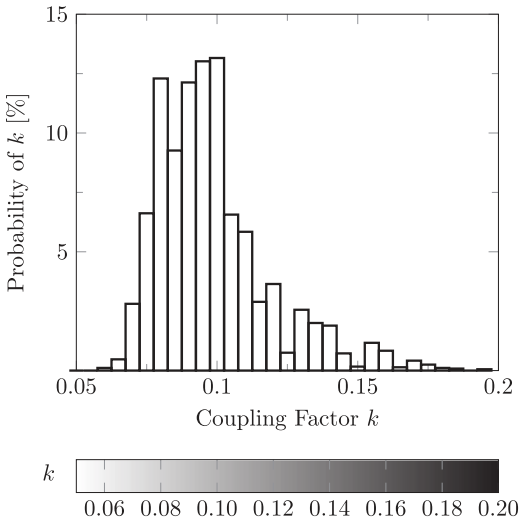

Fig. 8. Histogram of the coupling obtained from 3600 samples in 1 min.

thousand times lower than the SAR limit for the head and trunk, for general public exposure.

VI. Design of the Inverter: Load-Independent Class EF

The load-independent Class EF is a single-switch resonant inverter that outputs a sinusoidal current waveform that is independent of the load resistance. Also, unlike other single-switch resonant inverters, e.g., Class E [31], EF_2 [32], and Φ_2 [33], the load-independent inverter achieves zero-voltage switching (ZVS) for the entire resistive load range. A constant amplitude output current and ZVS are achieved inherently by designing the passives of the topology (see Fig. 10), as proposed in [21]. These equations rely on a fixed frequency of operation and a constant duty cycle of 30%, which is the value that achieves the highest power output capability of the transistor. Therefore, the inverter does not require a feedback loop to achieve load-independent operation.

TABLE II
SAR Limits for General Public and Occupational Exposure (W/kg)

	general public	occupational
Whole body average SAR	0.08	0.4
Localised SAR (head and trunk)	2	10
Localised SAR (limbs)	4	20

This inverter was chosen primarily because achieving high efficiency independent of the reflected load is very convenient when dealing with an IPT system in which k varies. Also, it allows the design of the transmitter and receiver to be done separately. The load-independent feature decouples the effects of the receiving-end on the transmitting-end, simplifying the dynamics of the system and allowing power throughput control to be implemented only at the receiving end. Moreover, i_{p} in (2) can be considered load-independent, as can $\mathcal{E}_{\mathrm{s}}(k, i_{\mathrm{p}})$. The transmitting-end functions as a load-independent alternating magnetic field generator, and the receiving end copes with power throughput control as k or power demand changes.

The design equations, selected from Table II in [21], are for the special case of maximum power output capability c_p, a ratio of the self-resonant frequency of L_2 and C_2, as shown in Fig. 10, q_1 of 1.66, and a ratio of C_1 and C_2 (denoted as k in [21]) of 1.2706, with a loading parameter p of 3. Thus, we have

$$\begin{aligned} 2\pi f_{i_{\mathrm{p}}} R_{\mathrm{eq_{max}}} C_1 &= 0.1096 \\ 2\pi f_{i_{\mathrm{p}}} C_1 X_{\mathrm{res}} &= 0.3403 \\ \frac{i_{\mathrm{p}} R_{\mathrm{eq_{max}}}}{V_{\mathrm{dc}}} &= 0.2938 \\ c_p &= 0.1096 \end{aligned} \tag{7}$$

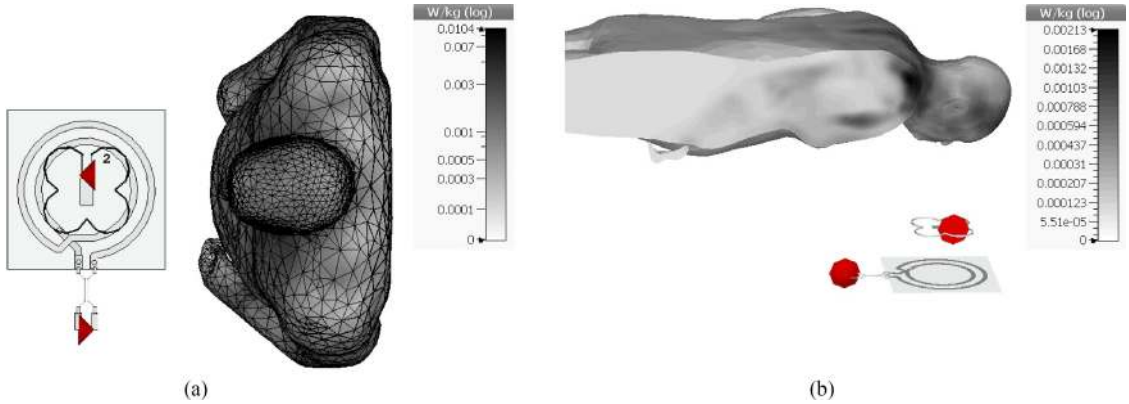

Fig. 9. SAR simulations with an $i_{\rm p}$ of 5.5 A. (a) Spectator watching from the side. (b) Spectator watching from above.

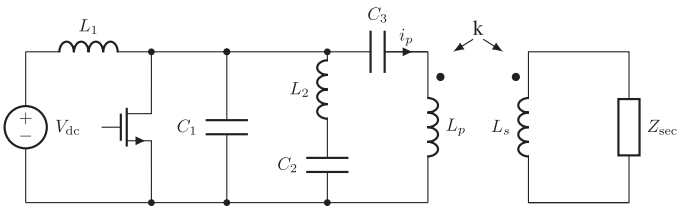

Fig. 10. Schematic of a Class EF inverter in an IPT system.

TABLE III
COMPONENT VALUES FOR THE INVERTER DESIGN

Component	Value	Description
C_1 (pF)	92+$C_{\rm oss}$	Vishay QUAD HIFREQ
C_2 (pF)	200	Vishay QUAD HIFREQ
C_3 (pF)	136	Vishay QUAD HIFREQ
L_1 (μH)	88	Wurth Elektronik WE-PD
L_2 (nH)	251	Coilcraft 2014VS
$R_{\rm eq_{max}}$ (Ω)	5.5	reflected resistance
Q_1	GS66504B (650 V, 15 A) GaN FET	

where $X_{\rm res}$ is the residual reactance given by

$$X_{\rm res} = 2\pi f_{i_{\rm p}} L_{\rm p} - \frac{1}{2\pi f_{i_{\rm p}} C_3}. \tag{8}$$

This set of equations is a practical solution to achieve load-independent operation while operating at a lower input voltage than in our first prototype [19] or the solutions presented in previous works using this tuning methodology for Class EF inverters [24], [34]–[36]. For this design, it is convenient to operate at a lower input voltage since the implemented dc power source is most likely to be of low voltage.

The component values used in this application are presented in Table III. Fig. 11 shows the experimental drain-voltage waveforms of the switch for a drone operating at different throttle values. It can be seen that, as expected, the drain voltage is zero at turn-ON ($f_{\rm i_p}\, t = 1$) for all the reflected-load cases.

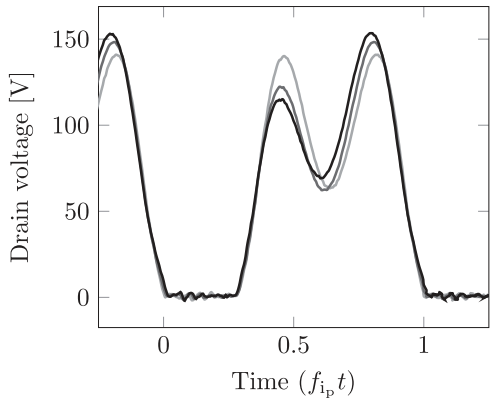

Fig. 11. Experimental waveforms of the drain voltage of the load-independent Class EF inverter while powering the wirelessly powered drone.

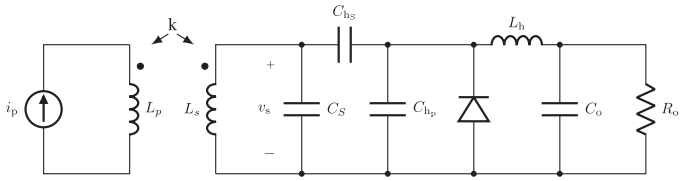

Fig. 12. Hybrid Class E rectifier in an IPT system.

VII. DESIGN OF THE RECTIFIER: HYBRID CLASS E

Various topologies were considered when selecting the rectifier for this system. We first implemented a half-wave current-driven Class D rectifier in [19], achieving good efficiencies at large air-gaps. However, the drone needed to remain fairly distant from the charging pad so as to not exceed the maximum input voltage of the dc–dc converter. In order to allow operating in broader ranges of k, we implemented a non-synchronous hybrid Class E rectifier that can be designed for low input reactance deviation as the load changes. An alternative solution based on a synchronous Class E rectifier is also mentioned in Section IX.

The hybrid Class E rectifier topology is shown in Fig. 12, coupled with the receiving-end coil $L_{\rm s}$ and a parallel capacitance $C_{\rm s}$ to resonate the coil. At the transmitting-end, there is a transmitting coil $L_{\rm p}$ and a current source $i_{\rm p}$ representing the inverter.

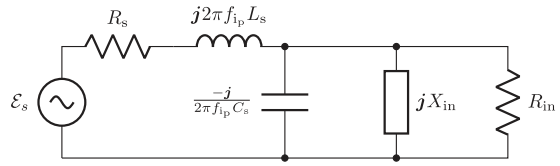

Fig. 13. Equivalent impedances of the receiving-end of an IPT system with the proposed impedance model of the hybrid Class E rectifier.

The benefits of this topology in comparison with other non-synchronous half-wave Class E rectifiers are discussed in [37], and the equations presented here are derived from that work.

The major restriction in the design of the rectifier for this application is the range of the output voltage of the rectifier, dictated by the tolerance of the components and, most importantly, by the range of input voltages of the following stage. The dc–dc converter chosen for this design, the LMZ14203 by Texas Instruments, allows input voltages from 6 to 42 V. Therefore, the output voltage of the rectifier V_o should remain within that range, considering the domain of $\mathcal{E}_s$ [see (2)] to assure an uninterrupted power flow and to avoid damaging the dc–dc converter.

The design process of the rectifier begins by selecting the point of k at which the link is to be optimized k_{opt} and by calculating the optimal load of the link at that point. For this parallel-tuned IPT system, the optimal load can be calculated as follows:

$$R_{ac_{opt}} = \frac{1}{2\pi f_{i_p} C_s - \frac{1}{X_{in}}} \left(\frac{Q_p}{\sqrt{1 + k_{opt}^2 Q_p Q_s}} \right) \tag{9}$$

where Q_p and Q_s are the Q-factors of the transmitting and receiving coils, respectively, and X_{in} is the input reactance (positive if inductive and negative if capacitive) of the rectifier. Equation (9) assumes the circuit shown in Fig. 13 to be at resonance.

k_{opt} was selected using the probability distribution shown in Fig. 8 in order to optimize the system in terms of efficiency at the most probable k. At this point, it is important to verify that the range of reflected resistance (3) and reactance (4) is within the range tolerated by the inverter for the entire range of k and P_o. After optimizing the link, the amplitude of i_p should be defined to provide the power required by the load P_o.

The design of the rectifier is relevant to achieve operation at the optimal load since the rectifier's ac–dc gain M_v can be determined by the passive components of the topology. The rectifier's input resistance R_{in}, which should be equal to the optimal load at k_{opt}, can be described as a function of the dc load R_o, which is the dc–dc converter's input resistance, given by

$$R_{ac_{opt}} = R_{in} = \frac{R_o}{2{M_V}^2}. \tag{10}$$

M_v depends on three parameters. First, it depends on the diode's duty cycle, which is strongly related to the loaded Q-factor of the rectifier, given by

$$Q_{rect} = \frac{R_o}{X_{rect}}. \tag{11}$$

X_{rect} is the reactance of $C_{h_p} + C_{h_s}$ given by

$$X_{rect} = \frac{1}{2\pi f_{i_p} \left(C_{h_p} + C_{h_s} \right)}. \tag{12}$$

The diode's duty cycle can, therefore, be designed by sizing the inductance L_h and the capacitance $C_{h_p} + C_{h_s}$ in accordance with the range of R_o.

Second, it depends on the ratio between the resonant frequency of the reactive elements of the rectifier and the frequency of operation given by

$$A_r = \frac{f_{rect}}{f_{i_p}} \tag{13}$$

where

$$f_{rect} = \frac{1}{2\pi \sqrt{L_h \left(C_{h_c} + C_{h_p} \right)}}. \tag{14}$$

Third, it depends on the ratio between the two capacitances of the topology given by

$$B = \frac{C_{h_p}}{C_{h_s}}. \tag{15}$$

The equation that describes M_v as a function of these variables can be found in Appendix A of [37].

In addition to designing the input resistance of the rectifier to be equal to the optimal load, the input reactance, along with how it changes as the coupling or power demand changes, has to be considered in the design of the rectifier. This can be done by representing the circuit connected to the receiving coil as a single impedance $\boldsymbol{Z_{sec}}$ (see Fig. 3) and can be calculated from the circuit shown in Fig. 13 as follows:

$$R_{sec} = \frac{1}{R_{in} \left(\frac{1}{R_{in}^2} + \left(\frac{1}{X_{C_s}} - \frac{1}{X_{in}} \right)^2 \right)} \tag{16}$$

$$X_{sec} = \left(\frac{1}{X_{in}} - \frac{1}{X_{C_s}} \right) \left(\frac{1}{\frac{1}{R_{in}^2} + \left(\frac{1}{X_{C_s}} - \frac{1}{X_{in}} \right)^2} \right) \tag{17}$$

considering that X_{in} is positive, if inductive, and negative, if capacitive. In order to achieve the maximum link efficiency at k_{opt}, X_{sec} has to be equal to $-2\pi f_{i_p} L_s$. However, since R_{in} and X_{in} change with load demand and $\mathcal{E}_s$, the link becomes slightly detuned when operating at a different point than the one of optimization. This feature can have a negative impact on the end-to-end efficiency as it slightly detunes the receiving-end when operating away from k_{opt}, but nonetheless, it allows operating at maximum coupling and minimum power without exceeding the voltage ratings of the dc–dc converter, significantly broadening the range of operation of the system.

The design variables of the rectifier are presented in Table IV, and the values of the components are presented in Table V.

TABLE IV
DESIGN VARIABLES FOR THE HYBRID CLASS E RECTIFIER

k_{opt}	M_{v}	d_{opt}	A_r	B
0.1	0.0519	0.4	0.3	0.95

TABLE V
DESIGN PARAMETERS AND COMPONENT VALUES OF THE RECTIFIER

Component	Value	Description
C_{p} (pF)	54	Vishay QUAD HIFREQ
C_{hs} (pF)	420	Vishay QUAD HIFREQ
C_{hp} (pF)	343+C_{oss}	Vishay QUAD HIFREQ
L_{h} (μH)	2.2	Coilcraft XAL40xx Series
C_{o} (μF)	20	AVX X7R
D	2x Cree C3D1P7060Q	

VIII. DESIGN VERIFICATION AND MEASUREMENTS

In order to provide the required power to the load, the amplitude of the current in the transmit coil can be determined using (5), evaluating R_{eq} at k_{opt} and maximum power. At this point, it is critical that the design is verified for the entire range of k and P_{o}, especially considering that η_{r} is also bound to change with these variables. The average power consumption of the drone was measured at full throttle and found to be 13 W, when fed from a 4.2-V dc source, and the most probable k, selected to be k_{opt} in this application, is 10%.

The output current amplitude of the inverter can be determined by changing the input voltage (7). However, large changes in input voltage may produce changes in C_1 due to the voltage-dependent output capacitance of the transistor. It is, therefore, recommended to tune the inverter for a specific voltage value, once the required i_{p} is determined. The input voltage of the inverter was set at 74 V, resulting in an i_{p} of approximately 3.8 A.

A. System Simulation

The behavior of the system was simulated using SPICE to verify its operation at the critical cases (k_{max} and $P_{\mathrm{o_{min}}}$, and k_{min} and $P_{\mathrm{o_{max}}}$) and the dynamic response between those cases, assuming step changes in load and k from minimum to maximum and conversely. The simulated circuit consists of a voltage source representing $\mathcal{E}_{\mathrm{s}}$, the passive components of the rectifier, and the off-the-shelf SPICE model of the dc–dc converter. The load was modeled as a resistor. The results of this simulation are shown in Fig. 14. The range of $V_{\mathrm{o_{reg}}}$ is well within the range of operation, considering that the drone without modification is fed from a battery, the voltage of which ranges from 4.2 to 3.7 V depending on the state of charge. The most critical value in this analysis is the range of V_{o}, which was verified to be within the boundaries allowed by the dc–dc converter, i.e., 42 and 6 V. Interestingly, if the dc–dc converter allowed a broader input voltage range, the system could operate at a broader range of k, resulting in higher spatial freedom.

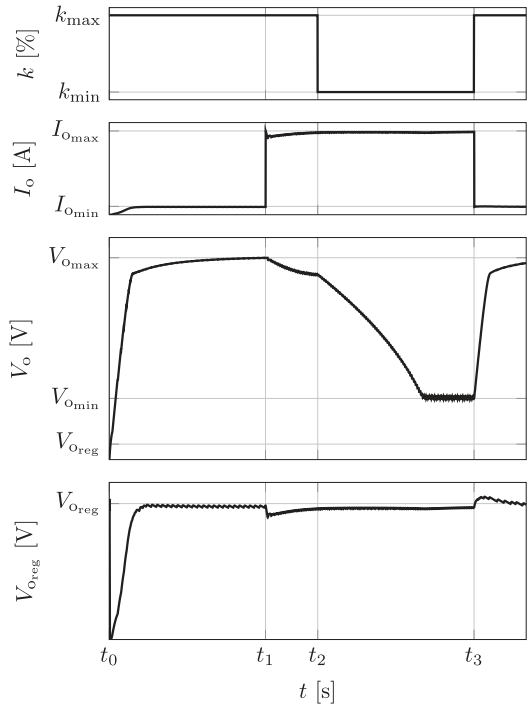

Fig. 14. SPICE simulation results performing step-changes between critical conditions in k and load resistance.

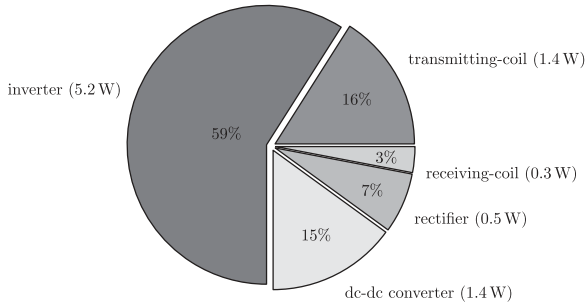

Fig. 15. Distribution of losses in the system from simulation.

B. System Performance

The average power consumption of the drone was measured and found to be 13.0 W, and the average input power of the inverter was measured and found to be 21.8 W; therefore, the average dc to regulated-dc efficiency is calculated to be 60%. The total losses on average, calculated at 8.8 W, are distributed, according to simulations, as shown in Fig. 15. The power consumption at the transmitting-end, when the system was driving the transmitting-coil without the drone, was measured and found to be 6.6 W; therefore, it can be assumed that the losses at the transmitting-end account for approximately 75% of the total losses since the losses in the load-independent Class EF inverter are fairly constant as the load varies due to its load-independent

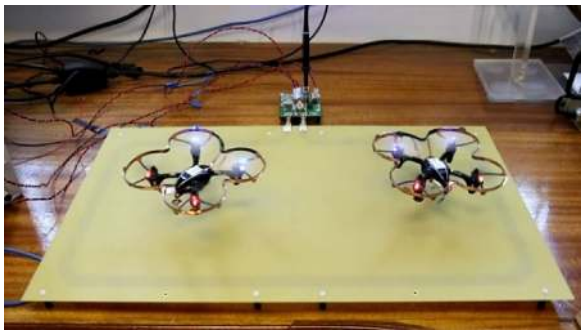

Fig. 16. Photograph of two wirelessly powered drones fed from a single transmitting-end.

Fig. 17. Photograph of the wireless charging drone.

switching performance. Also, since i_{p} is load-independent, the losses in the transmitting-coil do not change with load.

According to the calculations depicted in Fig. 15, the average link efficiency is 90%.

1) Thermal Considerations at the Transmitting-End: The inverter accounts for most of the power losses in the system. Most of the losses in this topology are in L_2 and the transistor [21]. The power losses in the transistor (estimated at 2 W) are dissipated through the board and a small heatsink attached to the bottom of the board. The temperature of the board remained well under 70 °C at no load, and it decreased when the load was operating because of the forced airflow produced by the drone.

2) Thermal Considerations at the Receiving-End: A small heatsink was added to the rectifier board since the temperature increased above 70 °C at low coupling and maximum throttle (i.e., low voltage and high current). The forward voltage of silicon carbide diodes tends to increase with temperature [38], and therefore, in order to achieve good efficiencies at low couplings, we designed for a maximum of 70 °C at the rectifier board. At maximum coupling and maximum throttle, the temperature of the diodes was much lower than 70 °C as they draw less current. This point, however, is critical to the dc–dc converter as the voltage ratio between the input and output terminals of the converter is at its maximum, resulting in a lower efficiency at this stage. The dc–dc converter could operate enclosed in the compartment that typically holds the battery without a heatsink.

IX. Other Demonstrations and Future Work

The demo described in this paper is the basis of various of our ongoing projects regarding lightweight solutions for highly variable coupling applications. An alternative design of the transmitting coil to wirelessly power drones without a battery is shown in Fig. 16. The coupling distribution of a system using this coil, comprised of a single-turn copper trace with a larger diameter, is steadier as the alignment of the coils changes. It can also feed power to multiple drones without batteries, simultaneously. It uses the same inverter with a slightly different tuning (slightly higher V_{dc} and a different C_3) as the one mentioned in Section VI, and the additional load to the inverter caused by the second drone did not require an additional heatsink or a fan. Coupling distribution and system optimization, as presented in Section IV, can be utilized for the design of the coils in order to obtain different specifications; for example, a lower variation in coupling in terms of linear misalignment.

A. Using Synchronous Rectification at the Receiving-End

A viable alternative to the hybrid Class E rectifier designed in Section VII is a synchronous Class E rectifier operating at a constant duty cycle. The benefits of this mode of operation are in avoiding very low duty cycles (less than 1%) when the power demand is at its minimum, which could be the case for any nonsynchronous Class E rectifier, and in having broader possibilities in the design of the reflected impedance of the rectifier as the load changes. For the wirelessly powered drone prototype, the rectifier was designed using the solutions for load-independent operation in [21] to have an output voltage that is independent of the load.

The solution implemented to trigger the operation of the transistor, which is difficult in this type of system, is detailed in [39].

The demo implementing the synchronous rectification solution draws more power from the source than the one that uses the hybrid Class E rectifier, mostly because of losses associated with driving the transistor, which in an application of such low power are not negligible. The synchronous rectifier can reflect a lower reactance to the transmitting-end than the hybrid Class E, thus avoiding detuning of the inverter at higher power demands. This, and the possible efficiency benefits of using a GaN transistor instead of a diode as the main switching device, suggests that this alternative might be more suitable for higher power applications.

B. Mounting the Transmitting-End on a Drone

The lightweight features of this technology are not limited to the receiving-end. Fig. 17 shows a drone with an on-board IPT transmitter, powered by the drone's battery. This IPT transmitter is capable of powering loads of up to 150 W; however, the power capability is mostly dictated by the drone's power supply (the drone uses a battery model TB47D-4500-22.2-6S from DJI that can output a maximum of 100 W continuously, including the power needed to operate the drone). We designed and built a dc–dc converter connected between the battery of the drone and the inverter to boost-up the voltage from 22.2 V to the voltage required by the inverter. This additional power conversion

stage can be used to regulate the intensity of the magnetic field produced by the on-board IPT transmitter as the input voltage dictates the amplitude of the current in the transmitting-coil (7). This system uses the same design as the one mentioned in Section VI, and the load in the experiment is an LED, representing a sensor positioned in environments with difficult access by other means [40], coupled with an IPT receiving-end that uses a hybrid Class E rectifier.

X. Conclusion

With newly developed resonant power converters and tuning methods, in addition to the advantageous features of wide bandgap devices, lightweight and efficient solutions for wireless power transfer using multi-MHz IPT are made possible.

The development of an IPT system capable of wirelessly powering a drone without a battery demonstrates efficient IPT while operating with substantial freedom of movement. The average end-to-end efficiency of the system was calculated to be 60% for a coupling factor ranging from 5.8% to 23.7%. Notwithstanding that this prototype was designed to power a 13-W load, a multi-MHz IPT can achieve dc–dc efficiencies higher than 80% for higher power loads. The coupling range could also be increased, potentially, in a less space-restrictive application than the one showcased in this paper.

The development of this system considers the requirements to showcase this technology and its capabilities to the public in a safe manner. The simulations of the SAR presented show that the magnetic field exposure to human tissues in this demo is more than 1000 times lower than the maximum allowed in the relevant guidelines.

References

[1] W. C. Brown, "Experiments involving a microwave beam to power and position a helicopter," *IEEE Trans. Aerosp. Electron. Syst.*, vol. AES-5, no. 5, pp. 692–702, Sep. 1969.

[2] G. A. Covic and J. T. Boys, "Modern trends in inductive power transfer for transportation applications," *IEEE Trans. Emerg. Sel. Topics Power Electron.*, vol. 1, no. 1, pp. 28–41, Mar. 2013.

[3] S. Li and C. C. Mi, "Wireless power transfer for electric vehicle applications," *IEEE Trans. Emerg. Sel. Topics Power Electron.*, vol. 3, no. 1, pp. 4–17, Mar. 2015.

[4] A. Zaheer, M. Neath, H. Z. Z. Beh, and G. A. Covic, "A dynamic EV charging system for slow moving traffic applications," *IEEE Trans. Transp. Electrific.*, vol. 3, no. 2, pp. 354–369, Jun. 2017.

[5] S. Y. R. Hui, W. Zhong, and C. K. Lee, "A critical review of recent progress in mid-range wireless power transfer," *IEEE Trans. Power Electron.*, vol. 29, no. 9, pp. 4500–4511, Sep. 2014.

[6] R. Bosshard, J. W. Kolar, J. Mhlethaler, I. Stevanovi, B. Wunsch, and F. Canales, "Modeling and η–α-Pareto optimization of inductive power transfer coils for electric vehicles," *IEEE Trans. Emerg. Sel. Topics Power Electron.*, vol. 3, no. 1, pp. 50–64, Mar. 2015.

[7] A. Kurs, A. Karalis, R. Moffatt, J. D. Joannopoulos, P. Fisher, and M. Soljačić, "Wireless power transfer via strongly coupled magnetic resonances," *Science*, vol. 317, no. 5834, pp. 83–86, 2007.

[8] K. Van Schuylenbergh and R. Puers, *Inductive Powering: Basic Theory and Application to Biomedical Systems*. Berlin/Heidelberg, Germany: Springer-Verlag, 2009.

[9] M. Pinuela, D. C. Yates, S. Lucyszyn, and P. D. Mitcheson, "Maximizing DC-to-load efficiency for inductive power transfer," *IEEE Trans. Power Electron.*, vol. 28, no. 5, pp. 2437–2447, May 2013.

[10] J. M. Arteaga, S. Aldhaher, G. Kkelis, D. C. Yates, and P. D. Mitcheson, "Multi-MHz IPT systems for variable coupling," *IEEE Trans. Power Electron.*, vol. 33, no. 9, pp. 7744–7758, Sep. 2018.

[11] J. Choi, D. Tsukiyama, Y. Tsuruda, and J. Rivas, "13.56 MHz 1.3 kW resonant converter with GaN FET for wireless power transfer," in *Proc. IEEE Wireless Power Transfer Conf.*, May 2015, pp. 1–4.

[12] A. Raciti, S. A. Rizzo, and G. Susinni, "Drone charging stations over the buildings based on a wireless power transfer system," in *Proc. IEEE/IAS 54th Ind. Commercial Power Syst. Tech. Conf.*, May 2018, pp. 1–6.

[13] U. K. Madawala and D. J. Thrimawithana, "New technique for inductive power transfer using a single controller," *IET Power Electron.*, vol. 5, no. 2, pp. 248–256, Feb. 2012.

[14] J. T. Boys, C.-Y. Huang, and G. A. Covic, "Single-phase unity power-factor inductive power transfer system," in *Proc. IEEE Power Electron. Specialists Conf.*, Jun. 2008, pp. 3701–3706.

[15] T. Diekhans and R. W. D. Doncker, "A dual-side controlled inductive power transfer system optimized for large coupling factor variations and partial load," *IEEE Trans. Power Electron.*, vol. 30, no. 11, pp. 6320–6328, Nov. 2015.

[16] M. K. Kazimierczuk and D. Czarkowski, *Resonant Power Converters*. New York, NY, USA: Wiley, 2012.

[17] M. Liu, S. Liu, and C. Ma, "A high-efficiency/output power and low-noise megahertz wireless power transfer system over a wide range of mutual inductance," *IEEE Trans. Microw. Theory Techn.*, vol. 65, no. 11, pp. 4317–4325, Nov. 2017.

[18] M. Hassanalian and A. Abdelkefi, "Classifications, applications, and design challenges of drones: A review," *Prog. Aerosp. Sci.*, vol. 91, pp. 99–131, 2017.

[19] S. Aldhaher, P. D. Mitcheson, J. M. Arteaga, G. Kkelis, and D. C. Yates, "Light-weight wireless power transfer for mid-air charging of drones," in *Proc. 11th Eur. Conf. Antennas Propag.*, Mar. 2017, pp. 1–5.

[20] J. M. Arteaga, G. Kkelis, S. Aldhaher, D. C. Yates, and P. D. Mitcheson, "Probability-based optimisation for a multi-MHz IPT system with variable coupling," in *Proc. IEEE PELS Workshop on Emerg. Technol.: Wireless Power*, Jun. 2018, pp. 1–5.

[21] S. Aldhaher, D. C. Yates, and P. D. Mitcheson, "Load-independent class E/EF inverters and rectifiers for MHz-switching applications," *IEEE Trans. Power Electron.*, vol. 33, no. 10, pp. 8270–8287, Oct. 2018.

[22] G. Kkelis, S. Aldhaher, J. M. Arteaga, D. C. Yates, and P. D. Mitcheson, "Hybrid class-E synchronous rectifier for wireless powering of quadcopters," in *Proc. IEEE Wireless Power Transfer Conf.*, May 2017, pp. 1–4.

[23] S. I. Babic and C. Akyel, "Calculating mutual inductance between circular coils with inclined axes in air," *IEEE Trans. Magn.*, vol. 44, no. 7, pp. 1743–1750, Jul. 2008.

[24] J. M. Arteaga, L. Lan, S. Aldhaher, G. Kkelis, D. C. Yates, and P. D. Mitcheson, "A multi-MHz IPT-link developed for load characterisation at highly variable coupling factor," in *Proc. IEEE Wireless Power Transfer Conf.*, Jun. 2018, pp. 1–4.

[25] W. B. Kuhn and A. P. Boutz, "Measuring and reporting high quality factors of inductors using vector network analyzers," *IEEE Trans. Microw. Theory Techn.*, vol. 58, no. 4, pp. 1046–1055, Apr. 2010.

[26] International Commission on Non-Ionizing Radiation Protection and others, "Guidelines for limiting exposure to time-varying electric, magnetic and electromagnetic fields," *Health Phys.*, vol. 74, pp. 494–522, 1998.

[27] International Commission on Non-Ionizing Radiation Protection and others, "Guidelines for limiting exposure to time-varying electric and magnetic fields (1 Hz to 100 kHz)," *Health Phys.*, vol. 99, no. 6, pp. 818–836, 2010.

[28] *IEEE Standard for Safety Levels With Respect to Human Exposure to Radio Frequency Electromagnetic Fields, 3 kHz to 300 GHz*, IEEE Standard C95.1-2005 (Revision of IEEE Standard C95.1-1991), Apr. 2006, pp. 1–238.

[29] A. Christ *et al.*, "Evaluation of wireless resonant power transfer systems with human electromagnetic exposure limits," *IEEE Trans. Electromagn. Compat.*, vol. 55, no. 2, pp. 265–274, Apr. 2013.

[30] J. Nadakuduti, M. Douglas, L. Lu, A. Christ, P. Guckian, and N. Kuster, "Compliance testing methodology for wireless power transfer systems," *IEEE Trans. Power Electron.*, vol. 30, no. 11, pp. 6264–6273, Nov. 2015.

[31] N. O. Sokal and A. D. Sokal, "Class E—A new class of high-efficiency tuned single-ended switching power amplifiers," *IEEE J. Solid-State Circuits*, vol. 10, no. 3, pp. 168–176, Jun. 1975.

[32] Z. Kaczmarczyk, "High-efficiency Class E, EF_2, and E/F_3 inverters," *IEEE Trans. Ind. Electron.*, vol. 53, no. 5, pp. 1584–1593, Oct. 2006.

[33] R. C. N. Pilawa-Podgurski, A. D. Sagneri, J. M. Rivas, D. I. Anderson, and D. J. Perreault, "Very-high-frequency resonant boost converters," *IEEE Trans. Power Electron.*, vol. 24, no. 6, pp. 1654–1665, Jun. 2009.

[34] S. Aldhaher, P. D. Mitcheson, and D. C. Yates, "Load-independent Class EF inverters for inductive wireless power transfer," in *Proc. IEEE Wireless Power Transfer Conf.*, May 2016, pp. 1–4.
[35] J. M. Arteaga, S. Aldhaher, G. Kkelis, D. C. Yates, and P. D. Mitcheson, "Design of a 13.56 MHz IPT system optimised for dynamic wireless charging environments," in *Proc. IEEE 2nd Annu. Southern Power Electron. Conf.*, Dec. 2016, pp. 1–6.
[36] A. Pacini, A. Costanzo, S. Aldhaher, and P. D. Mitcheson, "Load- and position-independent moving MHz WPT system based on GaN-distributed current sources," *IEEE Trans. Microw. Theory Techn.*, vol. 65, no. 12, pp. 5367–5376, Dec. 2017.
[37] G. Kkelis, D. C. Yates, and P. D. Mitcheson, "Class-E half-wave zero dv/dt rectifiers for inductive power transfer," *IEEE Trans. Power Electron.*, vol. 32, no. 11, pp. 8322–8337, Nov. 2017.
[38] S. Jahdi, O. Alatise, P. Alexakis, L. Ran, and P. Mawby, "The impact of temperature and switching rate on the dynamic characteristics of silicon carbide Schottky barrier diodes and MOSFETs," *IEEE Trans. Ind. Electron.*, vol. 62, no. 1, pp. 163–171, Jan. 2015.
[39] S. Aldhaher, D. C. Yates, and P. D. Mitcheson, "13.56 MHz 50 W load-independent synchronous class E rectifier using GaN devices for space-constrained applications," in *Proc. IEEE Wireless Power Transfer Conf.*, Jun. 2018, pp. 1–4.
[40] P. D. Mitcheson *et al.*, "Energy-autonomous sensing systems using drones," in *Proc. IEEE Sensors*, Oct.–Nov. 2017, pp. 1–3.

Juan M. Arteaga received the B.Sc. and Licentiate (Hons.) degrees in electrical engineering from the University of Costa Rica, San Pedro, Costa Rica, in 2008 and 2010, respectively, and the M.Sc. degree in micro and nanoelectronics from the Autonomous University of Barcelona, Bellaterra, Spain, in 2011. He is currently working toward the Ph.D. degree at the Imperial College London, London, U.K.

His research interests include power electronics, resonant converters, and wireless power transfer.

Samer Aldhaher received the B.Sc. degree in electrical engineering from the University of Jordan, Amman, Jordan, and the Ph.D. degree from Cranfield University, Bedford, U.K., in 2010 and 2014, respectively. His doctoral research focused on the design and optimization of switched-mode circuits and the development of novel electronic tuning methods for inductive power transfer applications.

He is currently a Research Associate with the Control and Power Group, Department of Electrical and Electronic Engineering, Imperial College London, London, U.K. His research interests include the design of multi-MHz dc/ac inverters and rectifiers and wireless power transfer applications based on resonant inductive links.

George Kkelis received the M.Eng. degree in electrical and electronic engineering from the University of Bristol, Bristol, U.K., and the Ph.D. degree in electrical and electronic engineering from the Imperial College London, London, U.K., in 2013 and 2018, respectively. His doctoral research focused on power electronics for optimization of multi-MHz inductive power transfer systems.

He is currently a Design Engineer with TMD Technologies Ltd., Hayes, U.K., working on high-voltage power supplies for traveling wave tube amplifiers.

Christopher Kwan received the M.Eng. degree in electrical and electronic engineering with management and the Ph.D. degree in electrical engineering from the Imperial College London, London, U.K., in 2013 and 2018, respectively. His doctoral research focused on the design of wireless power transfer systems in the presence of living objects and for implantable medical devices.

He is currently a Research Associate with the Control and Power Research Group, Department of Electrical and Electronic Engineering, Imperial College London, London, U.K. His research interests include the design and optimization of an inductive power transfer system for electric scooters/bicycles and medical implants.

David C. Yates (M'03) received the M.Eng. degree in electrical engineering and the Ph.D. degree from the Imperial College London, London, U.K., in 2001 and 2007, respectively. His doctoral research focused on ultralow power wireless links.

He is currently a Research Fellow with the Control and Power Group, Department of Electrical and Electronic Engineering, Imperial College London.

His research interests include converters and magnetics for wireless power transfers and ultralow-power RF circuits for sensor networks.

Paul D. Mitcheson (SM'12) received the M.Eng. degree in electrical and electronic engineering and the Ph.D. degree in micropower motion based energy harvesting for wireless sensor networks from the Imperial College London, London, U.K., in 2001 and 2005, respectively.

He is currently a Professor in electrical energy conversion with the Control and Power Research Group, Electrical and Electronic Engineering Department, Imperial College London. His research interests include energy harvesting, power electronics, and wireless power transfer to provide power to applications in circumstances where batteries and cables are not suitable. His research has been supported by the European Commission, Engineering and Physical Sciences Research Council, and several companies.

Dr. Mitcheson is a Fellow of the Higher Education Academy and is on the Executive Committee of the U.K. Power Electronics Centre.